Journal of Power Sources 415 (2019) 105–111

Contents lists available at ScienceDirect

Journal of Power Sources

journal homepage: www.elsevier.com/locate/jpowsour

High performance printable perovskite solar cells based on $Cs_{0.1}FA_{0.9}PbI_3$ in mesoporous scaffolds

Xiaomeng Hou[a,1], Mi Xu[a,1], Changheng Tong[a], Wenxian Ji[a], Zhengyang Fu[a], Zhining Wan[a], Fang Hao[b], Yue Ming[a], Shuang Liu[a], Yue Hu[a], Hongwei Han[a], Yaoguang Rong[a,*], Yan Yao[b,c,**]

[a] Michael Grätzel Center for Mesoscopic Solar Cells, Wuhan National Laboratory for Optoelectronics, China-EU Institute for Clean and Renewable Energy, Huazhong University of Science and Technology, Wuhan, 430074, Hubei, PR China
[b] Department of Electrical & Computer Engineering, University of Houston, Houston, TX, 77204, USA
[c] Texas Center for Superconductivity at the University of Houston, Houston, TX, 77204, USA

HIGHLIGHTS

- Printable perovskite solar cells enable efficient and low-cost photovoltaics.
- Understanding of crystal growth in constrained nanostructures is provided.
- The configuration offers a promising technical route for perovskite solar cells.

GRAPHICAL ABSTRACT

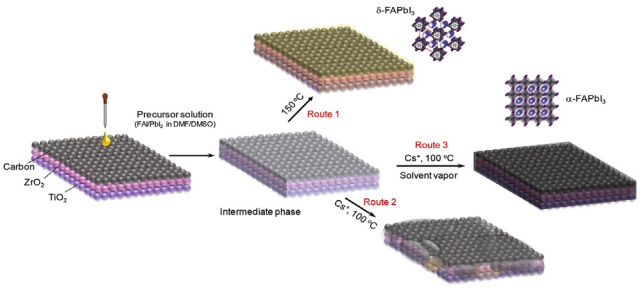

ARTICLE INFO

Keywords:
Perovskite solar cells
Mesoporous scaffold
$FAPbI_3$
Phase transition

ABSTRACT

Methylammonium lead triiodide ($MAPbI_3$) has been investigated as the recent most exciting light absorber materials for photovoltaics. Printable perovskite solar cells based on $MAPbI_3$ in a TiO_2/ZrO_2/Carbon triple-layer mesoporous scaffold have shown simple fabrication process and impressive stability. Moving towards formamidinium lead triiodide ($FAPbI_3$) as the light absorber, which has a bandgap of 1.48 eV that matches the optimum bandgap (1.34 eV) of a single-junction solar cell, will result in further improvement in power conversion efficiency. However, it is challenging to deposit high-quality $FAPbI_3$ in a 10-μm-thick mesoporous scaffold due to the incomplete one-step conversion of perovskite precursors restrained in the mesoporous scaffold. Here we report printable perovskite solar cells with high-quality $Cs_{0.1}FA_{0.9}PbI_3$ absorber inside mesoporous scaffolds using a mixed solvent vapor assisted crystallization approach. A power conversion efficiency of 15% is obtained with a spectral response up to 840 nm. The phase transition and crystal growth of $Cs_{0.1}FAPbI_3$ are carefully monitored in the mesoporous scaffold. This work not only opens up new methods for fabricating efficient and stable solar cells but also provides a deeper understanding of crystal growth inside constrained nanostructures.

* Corresponding author.
** Corresponding author. Department of Electrical & Computer Engineering, University of Houston, Houston, TX, 77204, USA.
E-mail addresses: ygrong@hust.edu.cn (Y. Rong), yyao4@uh.edu (Y. Yao).
[1] These authors contributed equally to this work.

https://doi.org/10.1016/j.jpowsour.2019.01.065
Received 21 July 2018; Received in revised form 12 December 2018; Accepted 23 January 2019
0378-7753/

1. Introduction

Perovskite solar cells (PSCs) have attracted intensive attention in the past several years, and the power conversion efficiency (PCE) of this photovoltaic technology has dramatically increased from 3.9% in 2009 to 23.3% [1–5]. The organic-inorganic hybrid perovskites possess unique properties as a light absorber for photovoltaics, such as suitable bandgaps, defect-tolerant bandstructures, high charge carrier mobility, small exciton binding energy, and long exciton diffusion length [6–8]. PSCs are usually fabricated by solution process and potentially low cost [9,10]. The most efficient PSCs usually utilize expensive hole-transport-materials (HTMs), such as 2,2′,7,7′-tetrakis(N,N-di-p-methoxy-phenylamine)-9,9′-spirobifluorene (spiro-OMeTAD) and poly(triaryl amine) (PTAA), as hole transporting layer with noble metal as the back contact [2,3,11]. Both the high material cost and energy-intensive thermal evaporation process prevent the large-scale production [8,12,13].

A hole-conductor-free printable mesoscopic PSC has recently been reported with a TiO_2/ZrO_2/Carbon triple-layer mesoporous scaffold [14–16]. Such PSCs could be fabricated using screen-printing technology [17], enabling low fabrication cost [8,18]. In addition, the hydrophobic mesoporous carbon layer protects the perovskite absorber from moisture penetration. With interface and compositional optimization [19], printable PSCs have demonstrated impressive stability under various conditions [16,20,21].

Compared with $MAPbI_3$ with a bandgap of 1.55 eV [5], formamidinium lead triiodide ($FAPbI_3$) has a lower bandgap of 1.48 eV, which is close to the optimum bandgap of 1.34 eV for a single-junction solar cell under typical sunlight conditions (unconcentrated, AM 1.5 solar spectrum) [22,23]. Besides, $FAPbI_3$ is thermally more stable than $MAPbI_3$ [24,25]. It is therefore strongly desired to infiltrate $FAPbI_3$ [26–28] into the triple-layer mesoporous scaffold to further improve the performance. The key challenge, however, is the incomplete conversion of the perovskite precursor to α-phase $FAPbI_3$, often forming non-perovskite δ-$FAPbI_3$ or unreacted PbI_2. Formamidinium cation (FA^+) possess a diameter of 1.9–2.2 Å, larger than that of methylammonium cation (MA^+, 1.8 Å). Significant volume expansion occurs during the formation of $FAPbI_3$ [28,29]. To deposit high-quality α-$FAPbI_3$ in the TiO_2/ZrO_2/Carbon triple-layer scaffold, we have previously reported a sequential two-step method, for which PbI_2 was first deposited and then a MAI/FAI solution bathing was applied [30]. It is critical to deposit a stoichiometric amount of PbI_2 into the mesoporous scaffold to avoid the incomplete conversion of PbI_2 in such two-step method. Most previous efforts to obtain high-quality $FAPbI_3$ thin films focus on the fabrication of conventional PSC architecture, which could not be directly applied to printable PSCs [28,29].

In this work, we reported printable PSCs based on high-quality perovskite $Cs_{0.1}FA_{0.9}PbI_3$ absorber in mesoporous scaffolds using a one-step mixed solvent vapor assisted crystallization approach. The phase transition and crystallization of $FAPbI_3$ in the scaffold could be tuned by solvent vapor annealing and printable PSCs show a PCE of 15% and a short-circuit current density of 23.63 mA cm^{-2}.

2. Experimental methods

2.1. Materials

Lead iodide (PbI_2), lead bromide ($PbBr_2$) and cesium iodide (CsI) were purchased from Sigma-Aldrich. Methylammonium iodide (MAI), Formamidinium iodide (FAI) and methylammonium bromide (MABr) were purchased from MaterWin Technology, China. The solvents of dimethylformamide (DMF) and dimethyl sulfoxide (DMSO) were purchased from Acros Organics. All the materials were used as received without further purification.

2.2. Device fabrication

FTO glass substrates were etched with a 1064 nm laser, and then ultrasonically cleaned with detergent, deionized water and ethanol for 10 min, respectively. A compact TiO_2 layer was deposited on the FTO substrates by spray pyrolysis deposition with di-isopropoxytitaniumbis (acetyl acetonate) solution at 450 °C. Subsequently the mesoporous TiO_2 layer (particle size 18 or 30 nm, GreatCell Solar), the ZrO_2 layer and carbon layer were deposited by screen-printing layer by layer, which were sintered at 500 °C, 500 °C and 400 °C for 30 min, respectively. After cooling down to room temperature, 2.0–3.0 μL perovskite precursor solution was dropped on the top of the carbon layer in ambient air or nitrogen filled glove box. After a thermal annealing (100–150 °C for 10–30 min) or a solvent vapor assisted annealing process (100 °C for 10 min), the device fabrication was finished. The compositions of the precursor solutions are presented in Table S1.

2.3. Characterization

Photocurrent density-voltage (*J-V*) characteristics were measured using a Keithley 2400 source/meter and a Newport solar simulator (model 91192-1000) giving light with AM 1.5 G spectral distribution, which was calibrated using a certified reference solar cell (Newport) to an intensity 100 mW cm^{-2}. A black mask with a circular aperture (diameter 3.6 mm, area 0.1 cm^2) was applied on top of the device. The scan rate is 150 mV s^{-1}. The incident photon-to-current conversion efficiency (IPCE) was performed using a 150 W xenon lamp (Oriel) fitted with a monochromator (Cornerstone 74004) as a monochromatic light source. Top-view and cross-sectional images of the perovskite films, scaffolds, and devices were measured on a field-emission scanning electron microscope (FE-SEM, Nova NanoSEM 450). The XRD spectra were measured with a Bruker D8 Advance X-ray diffractometer with Cu Ka radiation (λ = 1.5418 Å). The absorption spectrum of the perovskite films was recorded by UV-Vis-NIR spectrophotometer (UV-3600, Shimadzu Scientific Instruments) in the transmission mode. The optical microscope studies were conducted by metallographic microscope (DM2700M, Leica Microsystem) equipped with a CCD camera (Sony model Iris) connected to a PC. The steady-state photoluminescence spectra were carried out by LabRAM HR800 Roman Microscope. Perovskite films prepared on quartz were excited by laser beam at 532.16 nm. Time-resolved PL was measured at 760 nm using excitation with a 478 nm laser at a frequency of 4 MHz from the Horiba Jobin Yvon Fluoromax-4 fluorimeter. The lifetime was obtained by fitting the spectra with a biexponential decay function.

3. Results and discussion

Typical printable PSCs consist of a compact-TiO_2 (c-TiO_2) layer, a mesoporous TiO_2 layer, a ZrO_2 and a carbon layer (Fig. 1a) [16]. The mesoporous layers are deposited by a screen-printing process with thickness of 0.6, 2.0 and 10.0 μm, respectively. See detailed fabrication methods in the supporting information. The precursor solutions were prepared by dissolving FAI, PbI_2 in a single solvent of dimethylformaide (DMF) or a mixed solvent of DMF/dimethyl sulfoxide (DMSO). The concentrations and compositions of the precursors are described in Table S1. In previous work, we found that DMSO is able to coordinate with PbI_2 and form intermediate phase of $MA_2Pb_3I_8(DMSO)_2$, inducing crystallization of $MAPbI_3$ [31,32]. In the case of $FAPbI_3$ with larger cations, similar effect was also observed as shown in Fig. S1. For the precursor prepared with DMF, it is difficult to convert the mixture of FAI and PbI_2 into $FAPbI_3$ even after annealing at 150 °C for 30 min, showing a pale yellow color corresponding to unreacted PbI_2. When DMSO was used as a *co*-solvent in the precursor, the color turned from light yellow to orange, indicating the formation of δ-$FAPbI_3$ (*Route 1* in Fig. 1a). Considering the fact that MABr can stabilize α-$FAPbI_3$ [11], MABr and $PbBr_2$ were added in the precursor as additive.

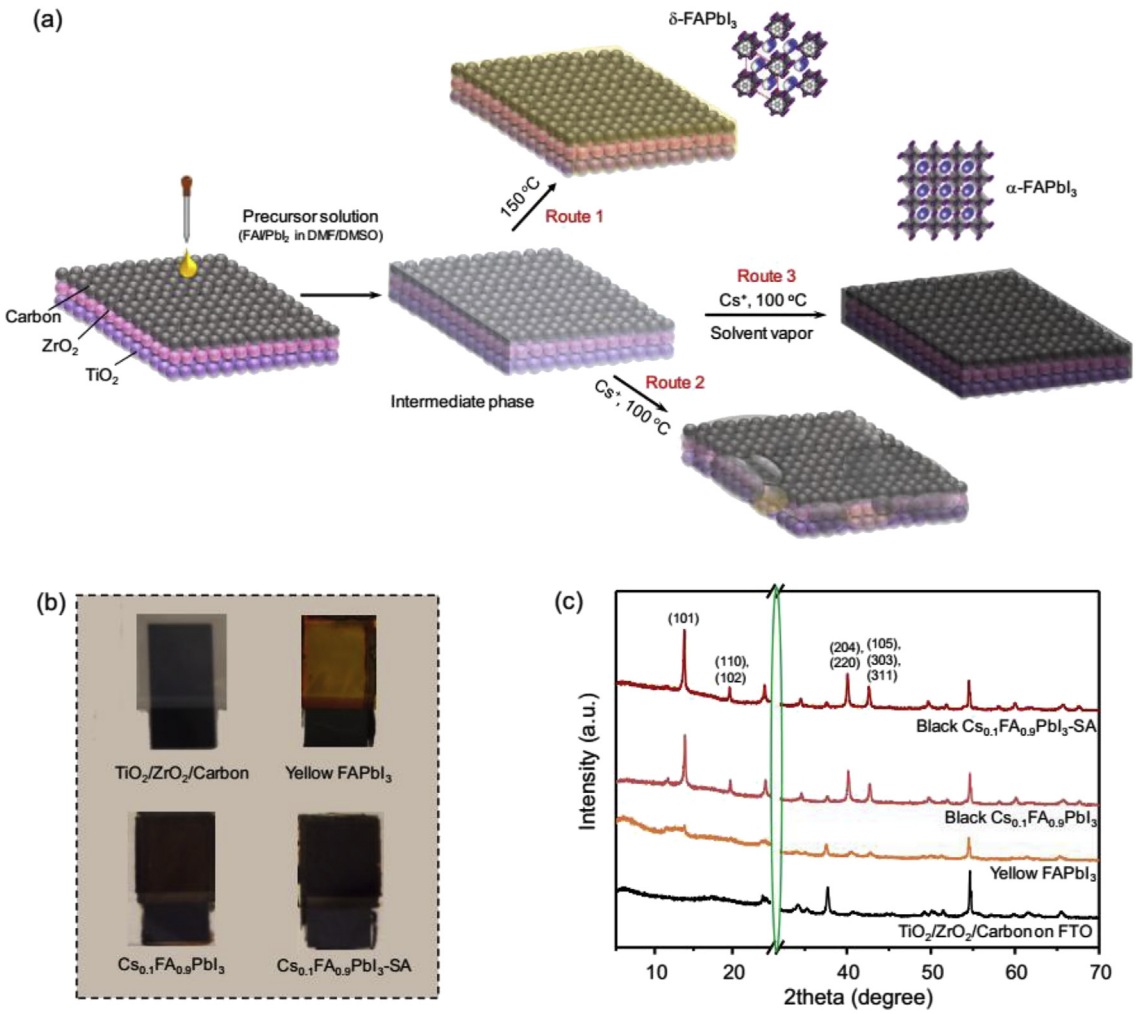

Fig. 1. Device configuration and deposition process of perovskite absorber. (a) The triple-layer scaffold of TiO_2/ZrO_2/Carbon is constructed by screen printing process, and the perovskite precursor solution (FAI/PbI_2 in a mixed solvent of DMF/DMSO with or without CsI) is drop-casted on the carbon layer. The scaffold is heated to 150 °C without CsI (Route 1), 100 °C with CsI (Route 2), or 100 °C with CsI and solvent vapor (Route 3). (b) images of blank, yellow $FAPbI_3$, $Cs_{0.1}FA_{0.9}PbI_3$ and $Cs_{0.1}FA_{0.9}PbI_3$-SA (solvent vapor) infiltrated mesoporous scaffold of TiO_2/ZrO_2/Carbon; (c) XRD patterns of blank, yellow $FAPbI_3$, $Cs_{0.1}FA_{0.9}PbI_3$ and $Cs_{0.1}FA_{0.9}PbI_3$-SA infiltrated mesoporous scaffold of TiO_2/ZrO_2/Carbon. (For interpretation of the references to color in this figure legend, the reader is referred to the Web version of this article.)

Unfortunately, this method did not work as expected (Fig. S1).

We found the challenge could be solved by incorporating CsI in the precursor solution [24], which leads to the formation of high-quality α-$Cs_{0.1}FA_{0.9}PbI_3$ phase inside the mesoporous scaffold (*Route 2* in Fig. 1a). Fig. 1b shows the digital images of a blank mesoporous scaffold, and a scaffold with yellow δ-$FAPbI_3$ infiltration, confirmed by X-ray diffraction (XRD) measurements (Fig. 1c) showing a tiny peak at 11.8°. After partially substituting FA^+ with Cs^+, the precursor can be easily converted into dark brown $Cs_{0.1}FA_{0.9}PbI_3$ by annealing at 100 °C, showing XRD peaks at 14.01°. Trace amount of δ-$FAPbI_3$ in the sample could still be observed according to the XRD pattern. Further treatment of the $Cs_{0.1}FA_{0.9}PbI_3$ infiltrated scaffold with DMF solvent vapor during the annealing process (*Route 3* in Fig. 1a) [33,34] could completely eliminate the undesired yellow δ-$FAPbI_3$ phase [33,34]. The concentrations and compositions of the precursors are described in Table S1.

It should be noted that successful conversion of the precursor to α-$FAPbI_3$ in the mesoporous scaffold not only relies on the incorporation of Cs^+ cation but also is attributed to the contribution of DMSO. Fig. S2 shows the comparison of XRD patterns of $Cs_{0.1}FA_{0.9}PbI_3$ obtained with a single solvent of DMF and a mixture solvent of DMF/DMSO. For the precursor based on DMF, the distinct peak at 11.8° corresponds to δ-$FAPbI_3$. While for the precursor based on DMF/DMSO, the peak at 11.8° (δ-$FAPbI_3$) almost disappeared, indicating a close to complete conversion from precursor to α-$FAPbI_3$ crystals. For the perovskite crystal growth *via* solution process, considerable volume expansion may occur when organic iodides (MAI or FAI) intercalates into the PbI_2 framework [35,36]. In the mesoporous scaffold of TiO_2/ZrO_2/Carbon, volume expansion is restrained due to the limited pore size, thus limiting phase transition of the perovskite absorber. It is therefore difficult to convert precursor to perovskite crystals. The two-step method has been proved an effective way to deposit perovskite in the printable mesoporous scaffold [30,37,38]. However, the ratio between PbI_2 and MAI/FAI cannot be precisely controlled. Here for the precursor based on the mixed solvent, DMSO molecular can coordinate with PbI_2 and form $PbI_2(DMSO)_2$ according to the ratio in the precursor [31,39]. During thermal annealing, FAI can exchange with DMSO inside the precursor. Since DMSO and FAI have similar size, this process will not lead to significant volume change, which facilitates the phase transition of $FAPbI_3$ in the mesoporous scaffold [40].

Besides the structural characterization of the phase transition, the morphology of $FAPbI_3$ in the mesoporous scaffold was analyzed by scanning electron microscopy (SEM). Cross-sectional SEM images of mesoporous scaffold TiO_2/ZrO_2/Carbon infiltrated with $Cs_{0.1}FA_{0.9}PbI_3$ and $Cs_{0.1}FA_{0.9}PbI_3$-SA are presented in Fig. 2a and b. In the mesoporous

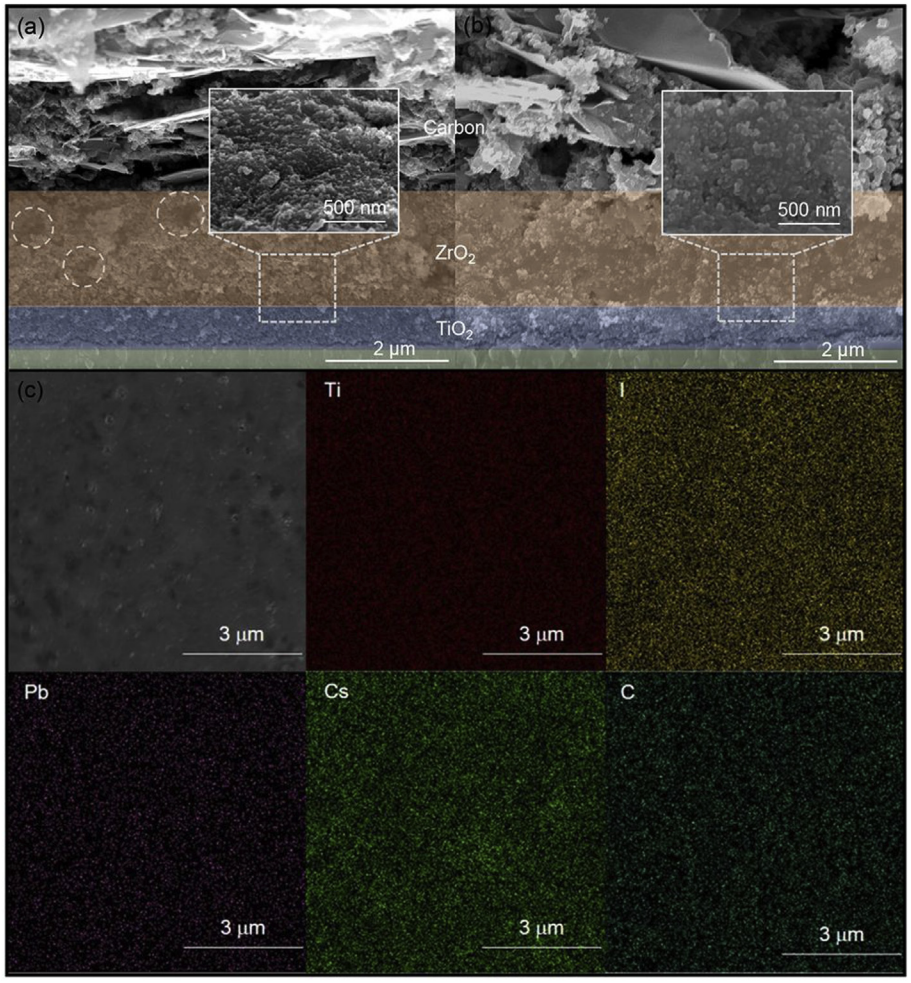

Fig. 2. Morphology characterization of the perovskite layer. Cross-sectional SEM images of mesoporous scaffold TiO_2/ZrO_2/Carbon infiltrated with $Cs_{0.1}FA_{0.9}PbI_3$ (a) and $Cs_{0.1}FA_{0.9}PbI_3$-SA (b). The insets show the morphology of perovskite crystals in the mesoporous TiO_2/ZrO_2 layers with high magnification. (c) the surface SEM image of $Cs_{0.1}FA_{0.9}PbI_3$-SA deposited on FTO/TiO_2/ZrO_2 substrate by spin coating, and the corresponding element distributions measured by energy dispersive spectrometer (EDS).

scaffold, $Cs_{0.1}FA_{0.9}PbI_3$ crystals were effectively deposited with interconnected morphology. Unfortunately, distinct unfilled nanopores were observed for $Cs_{0.1}FA_{0.9}PbI_3$ in the scaffold. When the solvent annealing process was employed, perovskite crystals could fill the pores completely and homogeneously (Fig. 2b). To confirm whether phase separation occurred for the mixed-cation perovskite, energy dispersive spectrometer (EDS) measurements were performed for $Cs_{0.1}FA_{0.9}PbI_3$-SA sample (Fig. 2c). The atoms of Ti, I, Pb, Cs and C homogeneously distributed in the film, indicating well-crystallized $Cs_{0.1}FA_{0.9}PbI_3$ in the mesoporous scaffold. The effect of Cs^+ on the morphology of the perovskite films was characterized using an optical microscope (Fig. S3). The activation free energy of formation of the black phase $FAPbI_3$ can be reduced by employing Cs^+ [41]. Thus, the crystallization of $Cs_{0.1}FA_{0.9}PbI_3$ was facilitated, resulting in faster crystal growth and much smaller domain size.

UV-visible absorption spectra and steady-state photoluminescence (PL) measurements were conducted to investigate the optical properties of $Cs_{0.1}FA_{0.9}PbI_3$, as shown in Fig. 3a. The samples were prepared by spin-coating at 5000 rpm, which can effectively avoid the formation of a capping layer over the mesoporous scaffold. Compared with typical perovskite $MAPbI_3$, the absorption onset of $Cs_{0.1}FA_{0.9}PbI_3$ reached 815 nm, which is consistent with previously reports [24,28]. The steady-state photoluminescence (PL) peak shifted from 774 nm to 798 nm. For $Cs_{0.1}FA_{0.9}PbI_3$ prepared by thermal annealing and solvent annealing (SA) process, the absorption spectra did not show much difference (Fig. S4) but an enhanced charge carrier lifetime was observed for solvent annealed sample (79.05 ns, Fig. 3b) from time-resolved photoluminescence (TRPL) measurements. These results indicated that SA process can effectively enhance crystallinity and reduce defect density of $Cs_{0.1}FA_{0.9}PbI_3$ crystals.

To fabricate efficient printable PSCs with well-crystallized $Cs_{0.1}FA_{0.9}PbI_3$, we first compared two commercial TiO_2 slurries (NR-18 and NR-30, GreatCell Solar). The photovoltaic parameters of the devices fabricated with NR-18 and NR-30 TiO_2 layer are summarized in Table 1. Due to the smaller pore size of NR-18 TiO_2 layer, it is difficult to convert the precursor to perovskite $Cs_{0.1}FA_{0.9}PbI_3$ completely. Thus, the devices showed much lower J_{SC} and fill factor (FF), which was related to the poor light absorption and charge transport in non-crystallized $Cs_{0.1}FA_{0.9}PbI_3$ mesoporous scaffolds. The series resistance (R_s) and shunt resistance (R_{sh}) of the devices are $\sim 19.83\,\Omega\,cm^2$ and $\sim 1.00\,k\Omega\,cm^2$. For the devices based on NR-30 TiO_2 layer, an average PCE of 13.93% could be obtained with an average J_{SC} of $22.92\,mA\,cm^{-2}$ and FF of 0.66. Correspondingly, the R_s decreased to $\sim 7.7\,\Omega\,cm^2$ and the R_{sh} increased to $\sim 2.19\,k\Omega\,cm^2$.

The spacer layer of ZrO_2 was also optimized for better performance. The mesoporous ZrO_2 layer works as an insulator between TiO_2 and carbon layer. When the ZrO_2 layer is too thin, the TiO_2 and carbon layer may directly contact, leading to voltage loss. On the contrary, when the ZrO_2 layer is too thick, the charge transport in the perovskite absorber will be limited. We compared the printable PSCs with three different

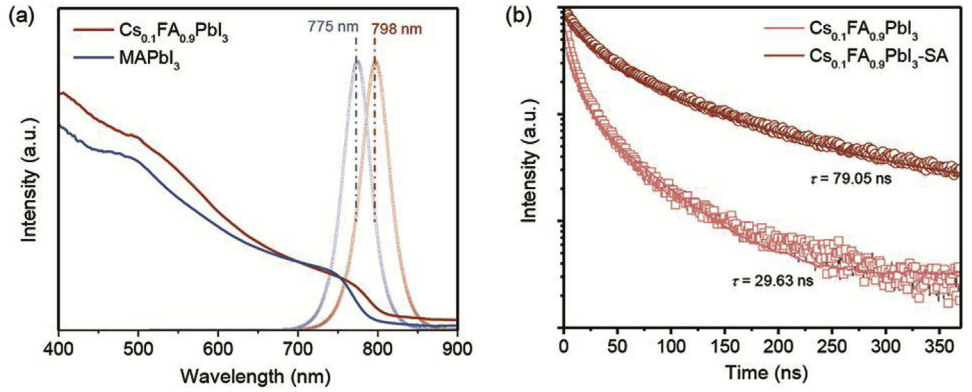

Fig. 3. Optical properties of perovskite absorber infiltrated in mesoporous scaffolds. (a) UV-Visible absorption spectra and steady-state photoluminescence (PL) spectra of $Cs_{0.1}FA_{0.9}PbI_3$ and $MAPbI_3$ on FTO/TiO_2 scaffold; (b) Time-resolved photoluminescence (TRPL) of $Cs_{0.1}FA_{0.9}PbI_3$ and $Cs_{0.1}FA_{0.9}PbI_3$-SA on glass/ZrO_2 scaffold.

thickness of ZrO_2 layer with the photovoltaic parameters summarized in Table 1. For ZrO_2 layer with a thickness of 1.2 μm, the devices showed an average PCE of 8.02%, with average open-circuit voltage (V_{OC}) of only 0.87 V, J_{SC} of 16.00 mA cm^{-2} and FF of 0.57. When the thickness of ZrO_2 layer was increased to 2.0 μm, the average PCE was improved to 14.38% along with enhanced V_{OC} of 0.91 V, J_{SC} of 23.03 mA cm^{-2} and FF of 0.66. For thicker ZrO_2 layer of 3.0 μm, the V_{OC} further increased from 0.91 V to 0.93 V, while the J_{SC} and FF both slightly decreased, leading to a significant decrease in PCE. We also attempted to employ Al_2O_3 as the insulating layer in printable PSCs [42,43]. Al_2O_3 has a much smaller particle size (Fig. S5) and stronger insulating ability. Our results show the devices employing Al_2O_3 as the spacer layer result a lower average PCE of 12.24% (Table S2). With the above optimization, we fixed the triple-layer mesoporous scaffold parameters as following: TiO_2 (particle size: 30 nm; thickness: 600 nm)/ZrO_2 (particle size:20 nm; thickness: 2.0 μm)/Carbon (thickness: 10 μm).

The *J-V* curve of the champion device using $Cs_{0.1}FA_{0.9}PbI_3$ as the light absorber is plotted in Fig. 4a, in which the typical perovskite $MAPbI_3$ was also included as a reference. The device based on $Cs_{0.1}FA_{0.9}PbI_3$ delivered a PCE of 15% with V_{OC} of 0.92 V, J_{SC} = 23.63 mA cm^{-2} and FF of 0.69. We also measured the device based on $MAPbI_3$ as a control device. A lower PCE of 9.65% was obtained with V_{OC} = 0.88 V, J_{SC} of 17.97 mA cm^{-2} and FF of 0.61. The device based on $Cs_{0.1}FA_{0.9}PbI_3$ showed broader spectral response that extended to 840 nm in comparison to that of $MAPbI_3$ (780 nm). The integrated J_{SC} values from the IPCE spectra was 22.01 mA cm^{-2} for $Cs_{0.1}FA_{0.9}PbI_3$, and 16.6 mA cm^{-2} for $MAPbI_3$ (Fig. 4b). Considering the slight hysteresis effect (Fig. S6), which could be caused by defective interface construction [44], steady-state output of the device was measured at a bias of 0.70 V to evaluate the accurate photovoltaic performance of the device (Fig. 4c). The stabilized current density was 20.71 mA cm^{-2}, and the corresponding PCE was 14.5%.

Considering the inspiring stability reported for the printable PSCs and moisture tolerance for the cesium containing perovskite [20,24], we performed a stability test in ambient air with a relative humidity (RH) of 30–50% at room temperature. The device was stored in the dark without encapsulation and tested every 48 h. Over a period of ~300 h, no distinct degradation of the photovoltaic parameters of the device was observed, as shown in Fig. 5a. Particularly, the device maintained 94.2% of initial PCE value. The devices based on $Cs_{0.1}FA_{0.9}PbI_3$ and $MAPbI_3$ were also heated up to 100 °C for 24 h. It was found that employing $Cs_{0.1}FA_{0.9}PbI_3$ as the light absorber of printable PSCs enabled much enhanced thermal stability, for which $Cs_{0.1}FA_{0.9}PbI_3$ in the mesoporous scaffold showed no color change during the thermal endurance test while $MAPbI_3$ faded after several hours and then decomposed to PbI_2 after 24 h at 100 °C.

4. Conclusion

In summary, we report printable perovskite solar cells with high-quality $Cs_{0.1}FA_{0.9}PbI_3$ absorber inside 10-μm-thick mesoporous scaffolds using a mixed solvent vapor assisted crystallization approach. The use of a mixed solvent and solvent annealing process effectively improved the crystallinity and reduced the defects in the perovskite absorber. Constructing $Cs_{0.1}FA_{0.9}PbI_3$ as the light harvesting material, the photovoltaic response of printable PSCs based on TiO_2/ZrO_2/Carbon architecture was extended to 840 nm, attaining a J_{SC} of 23.63 mA cm^{-2} and PCE of 15%. This work paves a way for enabling high-qualify perovskite crystal growth inside mesoporous scaffolds, and makes a step towards efficient printable mesoscopic PSCs using other perovskite absorbers besides $MAPbI_3$.

Conflicts of interest

There are no conflicts of interest to declare.

Acknowledgements

The authors acknowledge financial support from the National Natural Science Foundation of China (Grant No. 51502141, 91433203, 61474049 and 21702069), the Ministry of Science and Technology of China (863, 2015AA034601), the Fundamental Research Funds for the Central Universities, the Science and Technology Department of Hubei Province (No. 2017AAA190), the 111 Project (No. B07038), the China Postdoctoral Science Foundation (2017M612452), and the Double first-class research funding with independent intellectual property of ICARE. We thank the Analytical and Testing Center of Huazhong University of

Table 1
Photovoltaic parameters of printable PSCs fabricated with mesoporous TiO_2 layer of different particle size, and with ZrO_2 layer of different thickness.

Sample	V_{OC} (V)	J_{SC} (mA cm^{-2})	FF	PCE (%)	*Rs* (Ω cm^2)	*Rsh* (kΩ cm^2)
TiO_2-NR-18	0.94 ± 0.02	19.77 ± 0.10	0.50 ± 0.03	9.35 ± 0.80	19.83 ± 0.72	1.00 ± 0.28
TiO_2-NR-30	0.92 ± 0.02	22.92 ± 0.35	0.66 ± 0.20	13.93 ± 0.35	7.70 ± 0.15	2.19 ± 1.02
ZrO_2-1.2 μm	0.87 ± 0.01	16.00 ± 0.70	0.57 ± 0.02	8.02 ± 0.05	15.27 ± 1.12	0.25 ± 0.02
ZrO_2 -2.0 μm	0.91 ± 0.01	23.03 ± 0.60	0.66 ± 0.02	14.38 ± 0.60	6.92 ± 0.34	2.59 ± 0.87
ZrO_2 -3.0 μm	0.93 ± 0.01	21.85 ± 0.15	0.63 ± 0.01	12.74 ± 0.20	7.22 ± 0.19	1.66 ± 1.42

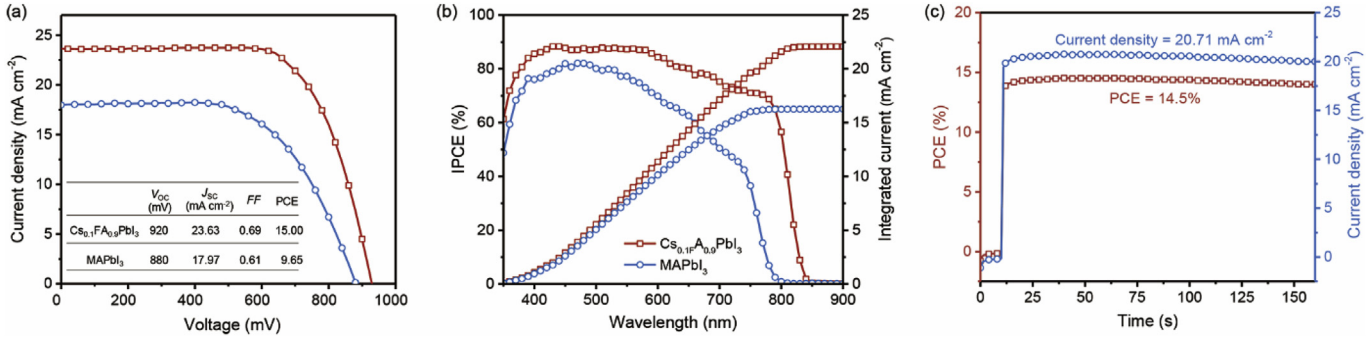

Fig. 4. Device performance characterization. (a) *J-V* curves of printable PSCs based on $Cs_{0.1}FA_{0.9}PbI_3$ and $MAPbI_3$; (b) IPCE spectra of printable PSCs based on $Cs_{0.1}FA_{0.9}PbI_3$ and $MAPbI_3$; (c) steady-state output of the device at a bias of 0.72 V.

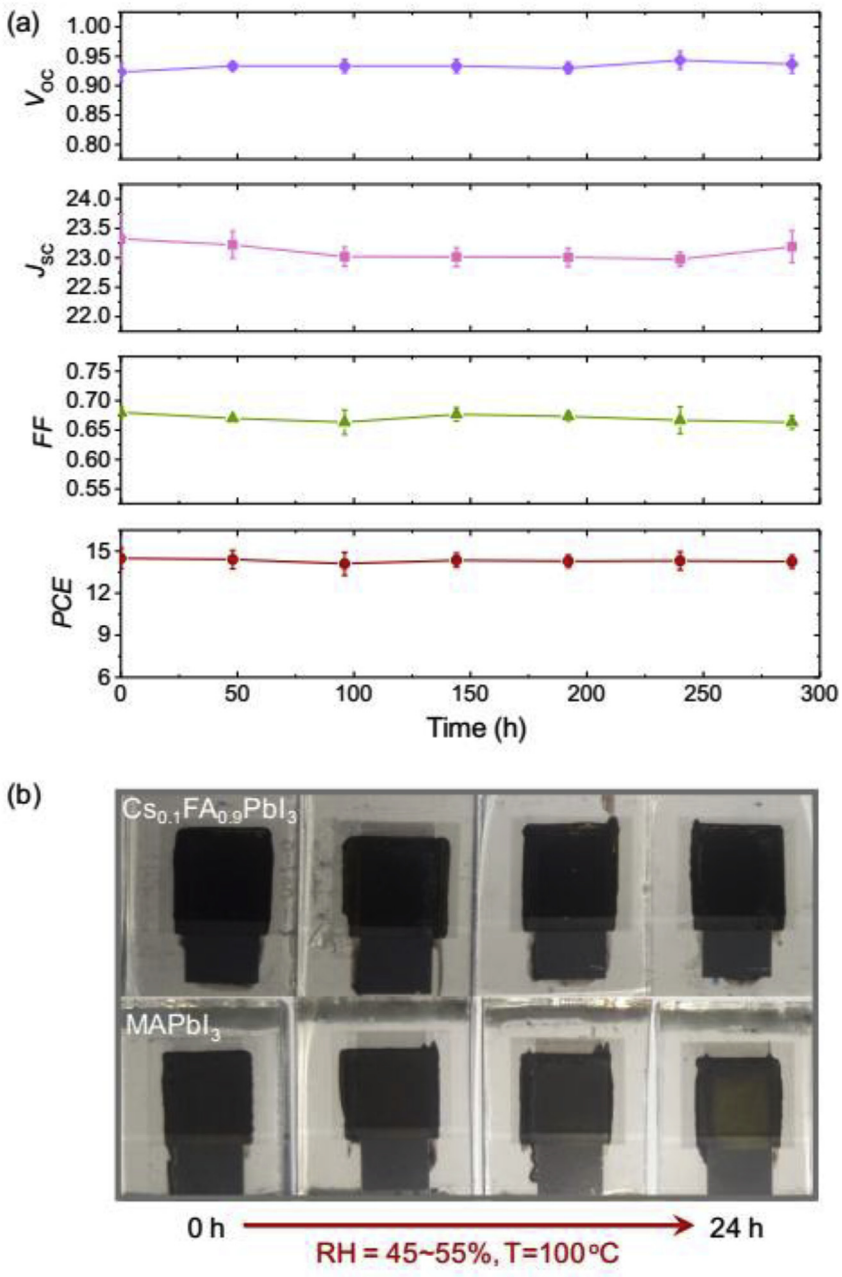

Fig. 5. Stability of printable PSCs. (a) The devices based on $Cs_{0.1}FA_{0.9}PbI_3$ were stored in ambient condition with relative humidity of 30–50% at room temperature for 300 h. The Error bars represent s.d. calculated from 3 devices prepared at the same conditions. (b) The devices based on $Cs_{0.1}FA_{0.9}PbI_3$ and $MAPbI_3$ were heated up to 100 °C with relative humidity of 45–55% for 24 h.

Science and Technology (HUST) for performing various characterization and measurements.

Appendix A. Supplementary data

Supplementary data to this article can be found online at https://doi.org/10.1016/j.jpowsour.2019.01.065.

References

[1] A. Kojima, K. Teshima, Y. Shirai, T. Miyasaka, J. Am. Chem. Soc. 131 (2009) 6050–6051.
[2] D. Bi, C. Yi, J. Luo, J.-D. Décoppet, F. Zhang, Shaik M. Zakeeruddin, X. Li, A. Hagfeldt, M. Grätzel, Nat. Energy 1 (2016) 16142.
[3] W.S. Yang, B.-W. Park, E.H. Jung, N.J. Jeon, Y.C. Kim, D.U. Lee, S.S. Shin, J. Seo, E.K. Kim, J.H. Noh, S.I. Seok, Science 356 (2017) 1376.
[4] Y. Rong, Y. Hu, A. Mei, H. Tan, M.I. Saidaminov, S.I. Seok, M.D. McGehee, E.H. Sargent, H. Han, Science (2018) 361.
[5] H.-S. Kim, C.-R. Lee, J.-H. Im, K.-B. Lee, T. Moehl, A. Marchioro, S.-J. Moon, R. Humphry-Baker, J.-H. Yum, J.E. Moser, M. Grätzel, N.-G. Park, Sci. Rep. 2 (2012) 591.
[6] G. Xing, N. Mathews, S. Sun, S.S. Lim, Y.M. Lam, M. Grätzel, S. Mhaisalkar, T.C. Sum, Science 342 (2013) 344–347.
[7] S.D. Stranks, G.E. Eperon, G. Grancini, C. Menelaou, M.J.P. Alcocer, T. Leijtens, L.M. Herz, A. Petrozza, H.J. Snaith, Science 342 (2013) 341–344.
[8] Y. Rong, L. Liu, A. Mei, X. Li, H. Han, Adv. Energy Mater. 5 (2015) 1501066.
[9] H.J. Snaith, J. Phys. Chem. Lett. 4 (2013) 3623–3630.
[10] M.A. Green, A. Ho-Baillie, H.J. Snaith, Nat. Photon. 8 (2014) 506–514.
[11] N.J. Jeon, J.H. Noh, W.S. Yang, Y.C. Kim, S. Ryu, J. Seo, S.I. Seok, Nature 517 (2015) 476–480.
[12] S.S. Shin, E.J. Yeom, W.S. Yang, S. Hur, M.G. Kim, J. Im, J. Seo, J.H. Noh, S.I. Seok, Science 356 (2017) 167–171.
[13] C. Bi, Q. Wang, Y. Shao, Y. Yuan, Z. Xiao, J. Huang, Nat. Commun. 6 (2015) 7747.
[14] Z. Ku, Y. Rong, M. Xu, T. Liu, H. Han, Sci. Rep. 3 (2013) 3132.
[15] Y. Rong, Z. Ku, A. Mei, T. Liu, M. Xu, S. Ko, X. Li, H. Han, J. Phys. Chem. Lett. 5 (2014) 2160–2164.
[16] A. Mei, X. Li, L. Liu, Z. Ku, T. Liu, Y. Rong, M. Xu, M. Hu, J. Chen, Y. Yang, M. Grätzel, H. Han, Science 345 (2014) 295–298.
[17] Y. Rong, H. Han, J. Nanophotonics 7 (2013) 073090-073090.
[18] Y. Rong, Y. Ming, W. Ji, D. Li, A. Mei, Y. Hu, H. Han, J. Phys. Chem. Lett. 9 (2018) 2707–2713.
[19] Y. Hu, Z. Zhang, A. Mei, Y. Jiang, X. Hou, Q. Wang, K. Du, Y. Rong, Y. Zhou, G. Xu, H. Han, Adv. Mater. 30 (2018) 1705786.
[20] Y. Rong, X. Hou, Y. Hu, A. Mei, L. Liu, P. Wang, H. Han, Nat. Commun. 8 (2017) 14555.
[21] Y. Hu, S. Si, A. Mei, Y. Rong, H. Liu, X. Li, H. Han, Solar RRL 1 (2017) 1600019.
[22] S. Rühle, Sol. Energy 130 (2016) 139–147.
[23] W. Shockley, H.J. Queisser, J. Appl. Phys. 32 (1961) 510–519.
[24] J.-W. Lee, D.-H. Kim, H.-S. Kim, S.-W. Seo, S.M. Cho, N.-G. Park, Adv. Energy Mater. 5 (2015) 1501310.
[25] S.-H. Turren-Cruz, A. Hagfeldt, M. Saliba, Science 362 (2018) 449–453.
[26] G.E. Eperon, S.D. Stranks, C. Menelaou, M.B. Johnston, L.M. Herz, H.J. Snaith, Energy Environ. Sci. 7 (2014) 982–988.
[27] Z. Wang, Y. Zhou, S. Pang, Z. Xiao, J. Zhang, W. Chai, H. Xu, Z. Liu, N.P. Padture, G. Cui, Chem. Mater. 27 (2015) 7149–7155.
[28] J.W. Lee, D.J. Seol, A.N. Cho, N.G. Park, Adv. Mater. 26 (2014) 4991–4998.
[29] Z. Zhou, S. Pang, F. Ji, B. Zhang, G. Cui, Chem. Commun. 52 (2016) 3828–3831.
[30] M. Hu, L. Liu, A. Mei, Y. Yang, T. Liu, H. Han, J. Mater. Chem. A 2 (2014) 17115–17121.
[31] Y. Rong, Z. Tang, Y. Zhao, X. Zhong, S. Venkatesan, H. Graham, M. Patton, Y. Jing, A.M. Guloy, Y. Yao, Nanoscale 7 (2015) 10595–10599.
[32] J. Chen, Y. Xiong, Y. Rong, A. Mei, Y. Sheng, P. Jiang, Y. Hu, X. Li, H. Han, Nano Energy 27 (2016) 130–137.
[33] Z. Xiao, Q. Dong, C. Bi, Y. Shao, Y. Yuan, J. Huang, Adv. Mater. 26 (2014) 6503–6509.
[34] H. Sun, X. Hou, Q. Wei, H. Liu, K. Yang, W. Wang, Q. An, Y. Rong, Chem. Commun. 52 (2016) 8099–8102.
[35] T. Liu, Q. Hu, J. Wu, K. Chen, L. Zhao, F. Liu, C. Wang, H. Lu, S. Jia, T. Russell, R. Zhu, Q. Gong, Adv. Energy Mater. 6 (2016) 1501890.
[36] W.S. Yang, J.H. Noh, N.J. Jeon, Y.C. Kim, S. Ryu, J. Seo, S.I. Seok, Science 348 (2015) 1234–1237.
[37] K. Cao, H. Li, S. Liu, J. Cui, Y. Shen, M. Wang, Nanoscale 8 (2016) 8839–8846.
[38] S. Liu, W. Huang, P. Liao, N. Pootrakulchote, H. Li, J. Lu, J. Li, F. Huang, X. Shai, X. Zhao, Y. Shen, Y.-B. Cheng, M. Wang, J. Mater. Chem. A 5 (2017) 22952–22958.
[39] H. Miyamae, Y. Numahata, M. Nagata, Chem. Lett. (1980) 663–664.
[40] Y. Rong, S. Venkatesan, R. Guo, Y. Wang, J. Bao, W. Li, Z. Fan, Y. Yao, Nanoscale 8 (2016) 12892–12899.
[41] C. Yi, J. Luo, S. Meloni, A. Boziki, N. Ashari-Astani, C. Gratzel, S.M. Zakeeruddin, U. Rothlisberger, M. Gratzel, Energy Environ. Sci. 9 (2016) 656–662.
[42] S. Liu, W. Huang, P. Liao, N. Pootrakulchote, H. Li, J. Lu, J. Li, F. Huang, X. Shai, X. Zhao, Y. Shen, Y.-B. Cheng, M. Wang, J. Mater. Chem. A 5 (2017) 22952–22958.
[43] K. Cao, Z. Zuo, J. Cui, Y. Shen, T. Moehl, S.M. Zakeeruddin, M. Grätzel, M. Wang, Nano Energy 17 (2015) 171–179.
[44] Y. Rong, Y. Hu, S. Ravishankar, H. Liu, X. Hou, Y. Sheng, A. Mei, Q. Wang, D. Li, M. Xu, J. Bisquert, H. Han, Energy Environ. Sci. 10 (2017) 2383–2391.